The unsteady three-dimensional wake produced by a trapezoidal pitching panel

Melissa A. Green†‡, Clarence W. Rowley and Alexander J. Smits

Department of Mechanical and Aerospace Engineering, Princeton University, Princeton, NJ 08544, USA

Particle image velocimetry (PIV) is used to investigate the three-dimensional wakes of rigid pitching panels with a trapezoidal geometry, chosen to model idealized fish caudal fins. Experiments are performed for Strouhal numbers from 0.17 to 0.56 for two different trailing edge pitching amplitudes. A Lagrangian coherent structure (LCS) analysis is employed to investigate the formation and evolution of the panel wake. A classic reverse von Kármán vortex street pattern is observed along the mid-span of the near wake, but the vortices realign and exhibit strong interactions near the spanwise edges of the wake. At higher Strouhal numbers, the complexity of the wake increases downstream of the trailing edge as the spanwise vortices spread transversely and lose coherence as the wake splits. This wake transition is shown to correspond to a qualitative change in the LCS pattern surrounding each vortex core, and can be identified as a quantitative event that is not dependent on arbitrary threshold levels. The location of this transition is observed to depend on both the pitching amplitude and free stream velocity, but is not constant for a fixed Strouhal number. On the panel surface, the trapezoidal planform geometry is observed to create additional vortices along the swept edges that retain coherence for low Strouhal numbers or high sweep angles. These additional swept-edge structures are conjectured to add to the complex three-dimensional flow near the tips of the panel.

Key words: swimming/flying, vortex dynamics, vortex streets

1. Introduction

The locomotion of fish and aquatic animals is acheived by the oscillation of their fins and flukes, which creates highly three-dimensional, unsteady flow fields that are characterized by coherent vortices shed by the trailing edge. Previous two-dimensional experiments have shown that the unsteady motion typically generates two counter-rotating spanwise vortices at the trailing edge during each flapping cycle, referred to as a 2S wake (Williamson & Roshko 1988; Koochesfahani 1989). In a thrust-producing scenario, these vortices are arranged in a reverse von Kármán vortex street, with the vortices aligned such that the induced velocity is directed downstream, adding momentum to the flow.

† Email address for correspondence: magreen@lcp.nrl.navy.mil

‡ Present address: Laboratory for Computational Physics and Fluid Dynamics, Naval Research Laboratory, Washington, DC 20375, USA.

The non-dimensional parameters governing unsteady flows developed by two-dimensional rigid foils are the Reynolds number and the Strouhal number. The Reynolds number is typically defined as $Re = Uc/\nu$, where U is the free stream velocity, c is the chord length and ν is the fluid kinematic viscosity. The Strouhal number is given by $St = fA/U$, where f is the frequency of oscillation and A is the width of the wake, commonly approximated as the peak-to-peak amplitude of the trailing edge. As long as the Reynolds number is sufficiently high ($O(1000)$), it plays a relatively minor role, and the Strouhal number is the dominant parameter. Triantafyllou, Triantafyllou & Grosenbaugh (1993) used a linear stability analysis on the wake of an oscillating foil to predict St for optimal propulsive efficiency and found that it lies in the range $0.25 \leqslant St \leqslant 0.35$. This was confirmed by the results obtained from a two-dimensional flapping foil experiment, and the authors also showed that, for moderate Re, many marine animals swim in a Strouhal number range of $0.2 < St < 0.4$. Later work has shown that in the viscous regime, the self-propulsion of swimming bodies occurs at even higher Strouhal numbers (Lauder & Tytell 2006; Borazjani & Sotiropoulos 2008; Tytell *et al.* 2010), but for the current work, the optimal range for moderate Re swimming is relevant.

Experiments and computations on pitching and flapping bodies of finite aspect ratio have revealed that the three-dimensional wake structure is considerably more complex than the two-dimensional case, and that its form is a strong function of both the Strouhal number and aspect ratio AR ($=S/c$, where S is the span and c is the chord) (von Ellenrieder, Parker & Soria 2003; Guglielmini 2004; Dong *et al.* 2005; Ghovardhan & Williamson 2005; Sarkar & Venkatraman 2006; Zhu & Shoele 2008; Green & Smits 2008). Buchholz (2006) performed flow visualization experiments on a series of low-aspect-ratio propulsors and found that with increasing Strouhal number or decreasing aspect ratio, the wake transitions from the 2S configuration to a 2P configuration, where two pairs of opposite sign vortices are shed during each pitching cycle. Each pair shifts transversely with their induced velocity, effectively splitting the wake. Hultmark, Leftwich & Smits (2007) also found that in the wake of an undulatory swimmer the vorticity spreads transversely and splits into two pairs of vortices per cycle. Buchholz, Green & Smits (2010) and Buchholz & Smits (2008) proposed that the structure of the wake downstream of the trailing edge was established by the distribution of vorticity on the panel surface before the vortices were shed, whereas Dabiri (2009) argued that for a wide range of biological propulsors the wake creation is governed by optimal vortex formation theory.

Regardless of the mechanism by which these bio-inspired wakes transition from a 2S to a 2P configuration, the transition occurs very close to, if not within, the range of Strouhal numbers at which Triantafyllou *et al.* (1993) reported that fish swim. Buchholz & Smits (2008) and Clark & Smits (2006) reported peak efficiencies in the range $0.1 < St < 0.3$ for a rectangular pitching panel and a batoid-inspired fin, respectively. In both cases, the peak efficiency was shown to correspond to a 2S wake structure, but that the transition to 2P occurred at only slightly higher St. For one set of parameters, Buchholz & Smits (2008) saw peak efficiency at $St = 0.21$ and transition by $St = 0.41$. Clark & Smits (2006) reported peak efficiency at $St = 0.25$ and transition by $St = 0.3$. Curves of efficiency versus Strouhal number in both cases had a shallower slope for $St > St_{\eta,max}$. Therefore, the wake bifurcation was not associated with a drastic loss of efficiency. Considering that both of these wakes are observed for St at which fish swim, and the point of transition is relatively close to that of peak efficiency, the transition is of special interest for understanding efficient steady swimming.

In the current work we use a rigid flat plate of trapezoidal planform geometry in purely pitching motion to approximate a simple fish caudal fin (tail) shape and motion. We use both Eulerian and Lagrangian analyses not only to visualize, but to analyse the evolution of coherent structures downstream of the panel trailing edge and its dependence on Strouhal number. Our principal aims also include an investigation into the effects of the trapezoidal planform on the formation of the fully three-dimensional, unsteady wake. We study the mechanisms which generate 2S and 2P wakes using a Lagrangian coherent structure (LCS) analysis, which has been shown to be a frame-independent method that is virtually independent of thresholding.

2. Lagrangian analysis

To investigate the vortex-dominated wakes of bio-inspired propulsors, we use a Lagrangian analysis. Previous work on flow structure identification has primarily used Eulerian criteria, which evaluate the spatial structure of quantities derived from the instantaneous velocity field and its gradient. Examples of Eulerian criteria include the Q criterion of Hunt, Wray & Moin (1988), the swirl strength (λ_{ci}^2) of Zhou *et al.* (1999), the Δ criterion of Chong, Perry & Cantwell (1990) and the λ_2 criterion of Jeong & Hussein (1995). These measures yield similar results when used to study the same flow, but they all share some general disadvantages. For example, although they are invariant with respect to Galilean transformations, they are not invariant to time-dependent rotations, and thus are not objective (frame independent) (Haller 2005). Furthermore, Eulerian criteria require a user-defined threshold to indicate the regions where a flow structure exists, which always introduces a level of ambiguity in the definition of the structure itself.

In contrast, more recent Lagrangian methods, such as LCS or the M_Z criterion of Haller (2005), identify coherent structures based on the flow properties along fluid particle trajectories. An immediate advantage of these methods is their objectivity: they are frame independent. A further advantage of Lagrangian methods is their insensitivity to short-term anomalies in the velocity field. For instance, finite-time Lyapunov exponent (FTLE) fields, often used to determine LCSs from discrete data, have been shown to be robust and relatively insensitive to imperfect velocity data as long as the errors remain small in a special time-weighted norm (Haller 2002). For this reason, LCS analyses perform well for experimental data, and they are not restricted to analytically defined velocity fields or finely resolved computational cases. By contrast, the Eulerian criteria involve velocity gradients, which cannot be computed accurately if the velocity data is noisy or coarsely resolved.

LCS analysis has increasingly gained popularity as a coherent structure identification tool, and it has been primarily applied to incompressible flows. In two-dimensional planar flows, Lekien & Leonard (2004) performed an LCS analysis to find coherent structures in order to assist in glider trajectory planning in the currents of Monterey Bay, and Shadden, Dabiri & Marsden (2006) and Shadden *et al.* (2007) and O'Farrell & Dabiri (2010) employed FTLE to identify a similar vortex ring wake structure produced by pistons and by swimming jellyfish using two-dimensional digital particle image velocimetry (DPIV) data. FTLE has also been used as a structure identification tool in two-dimensional quasi-geostrophic turbulence (Haller & Yuan 2000), freely decaying two-dimensional turbulence (Lapeyre 2002), a vortex-shedding two-dimensional aerofoil (Lipinski, Cardwell & Mohseni 2008), flapping two-dimensional wing simulations (Eldredge & Chong 2010) and LIDAR measurements of the airspace around Hong Kong International Airport (Tang, Chan & Haller 2010).

In three dimensions, FTLE has been computed by Haller (2005) on two established analytic flow solutions, Shadden, Astorino & Gerbeau (2010) and Shadden & Taylor (2008) performed an LCS analysis on three-dimensional computational solutions of the blood flow through aortic valves and abdominal aortic aneurysms and Green, Rowley & Haller (2007) described structure composition and evolution of an isolated hairpin vortex and a fully turbulent channel flow.

We investigate LCSs by calculating the FTLE scalar field, a quantity calculated at each point in space that is a measure of the maximum rate of separation among neighbouring particle trajectories initialized near that point. Large values of the FTLE field may indicate locally maximal stretching among particle trajectories, and ridges in the FTLE field are referred to as the LCS. The LCSs are nearly material lines that move with the local convective velocity with finite, but small, flux across them (Shadden, Lekien & Marsden 2005). Trajectories that stretch relative to each other when integrated in negative (backward) time converge in positive (forward) time. Therefore, by integrating particle trajectories in both positive and negative time we can calculate positive- and negative-time FTLE fields (pFTLE and nFTLE, respectively), from which we extract the positive- and negative-time LCSs (pLCS and nLCS, respectively). These structures are candidate repelling (pLCS) and attracting (nLCS) material lines, and can delineate the boundaries between qualitatively different regions in a flow (Shadden *et al.* 2006).

More recently, Haller (2010) has exposed some of the vulnerabilities associated with only using the ridges of the FTLE fields, and showed that not all LCSs are FTLE ridges, and that not all FTLE ridges depict natural LCSs in the flow. While we do not apply the new formalism of Haller (2010) in identifying hyperbolic LCSs in this paper, we check for local strain near the FTLE ridges to indicate hyperbolic stretching (as opposed to shear stretching) (Haller 2002). Specifically, we compute the rate of strain normal to the surface of the LCS, given by $\langle \boldsymbol{n}, \boldsymbol{Sn} \rangle$, where $\boldsymbol{n}$ is the unit normal to the LCS, and $\boldsymbol{S}$ is the rate of strain tensor given by

$$S_{ij} = \frac{1}{2} \left(\frac{\partial u_i}{\partial x_j} + \frac{\partial u_j}{\partial x_i} \right). \tag{2.1}$$

We confirm a ridge to be an attracting material line if the strain rate normal to the nLCS surface is negative. Similarly, we confirm a ridge to be a repelling material line if the strain rate normal to the pLCS surface is positive.

The LCS shown here are visualized as ridges of the FTLE field above a threshold chosen to reveal the complete structure boundary, and those regions in which the FTLE fields do not satisfy the hyperbolicity criteria are left blank. Thresholds were chosen so that the representations of coherent structures were as clear and complete as possible. The location, shape and size of coherent structures are unaffected by the threshold value, and do not affect the conclusions drawn from these results.

3. Experimental apparatus

A water channel was used to investigate the three-dimensional structure of the wake generated by pitching rigid panels. The panels were of trapezoidal planform to study the effects of the swept edge commonly seen in aquatic animal caudal fins. Flow visualization was used to determine the large-scale flow characteristics, and DPIV was used to reconstruct the full three-dimensional wake from a collection of two-dimensional planes.

Panel	c (mm)	S (mm)	θ (deg.)
1	70	175	45
2	90	213	45
3	100	168	30

TABLE 1. Trapezoidal panel geometries.

The test section of the water channel was 0.46 m wide and 0.29 m deep. An acrylic plate, 12 mm thick and 1.22 m long, was used to cover the free surface and prevent the formation of surface waves which would influence the flow in the test section and distort the flow imaging from above. Experiments were conducted with flow velocities in the range of 0.012 m s^{-1} < U < 0.3 m s^{-1}, corresponding to chord Reynolds numbers of 4200–14 000. Over this range of Reynolds numbers, viscous effects are not expected to be important.

Upstream of the test section, a honeycomb flow straightener, two screens and a 5:1 contraction were used to condition the flow. To maintain good flow quality, the honeycomb and screens were routinely cleared of bubbles and particles, and the screens were periodically removed entirely to clear the accumulation of particles and other sediment.

The pitching panels were attached at the leading edge to a 4.76 mm diameter pitching shaft. The angular position of the panel was given by a 2048 count-per-revolution quadrature encoder (US Digital model E3-2048-187-IH) mounted to the pitching shaft, thereby providing phase information. To support the pitching apparatus, the shaft was attached to the trailing edge of a hollow symmetric fairing based on a NACA 0012-64 aerofoil, as described by Buchholz & Smits (2008), and shown in figure 2(*a*). The fairing had a chord length of 50.8 mm and the trailing edge was truncated to allow the attachment of the pitching shaft. Tapered NACA 0012-64 aerofoil trailing edge segments were mounted behind the pitching shaft when the finite aspect ratio panels were in use. While this mitigated the vortex shedding from the cylindrical pitching shaft, shedding could not be entirely suppressed at low speeds (high Strouhal number).

The panel and the fairing were mounted vertically in the water channel test section. Positive streamwise distance ($+x$) is measured downstream of the trailing edge. The actuation of the panel used the same mechanism as in Buchholz (2006), which achieved the pitching motion using the four-bar linkage shown in figure 2(*b*). The trailing edge pitching amplitude could be changed by adjusting the distance between the crank shaft and the pitching shaft using a linear traverse.

The rigid panels used in these experiments had a trapezoidal planform with swept edges that were set at an angle from the streamwise direction. A schematic of the generalized panel is shown in figure 1, and a summary of the geometrical parameters describing the panels used in the DPIV and flow visualization experiments is given in table 1.

The experimental conditions are summarized in table 2. Three-dimensional experiments were conducted using panel 1 at Strouhal numbers of 0.17 and 0.28 with a trailing edge pitching amplitude of 10 mm, and a pitching frequency of 1 Hz. Additional data (two-dimensional) were obtained in a single plane at the midspan of the panel pitching at 1 Hz with a trailing edge amplitude of 20 mm, for four Strouhal numbers between 0.17 and 0.56. Lastly, a set of flow visualization experiments were
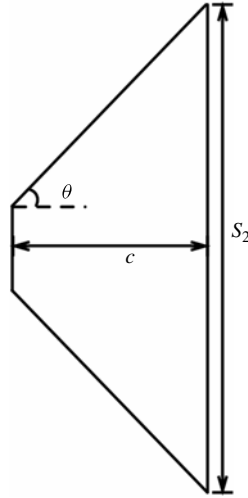
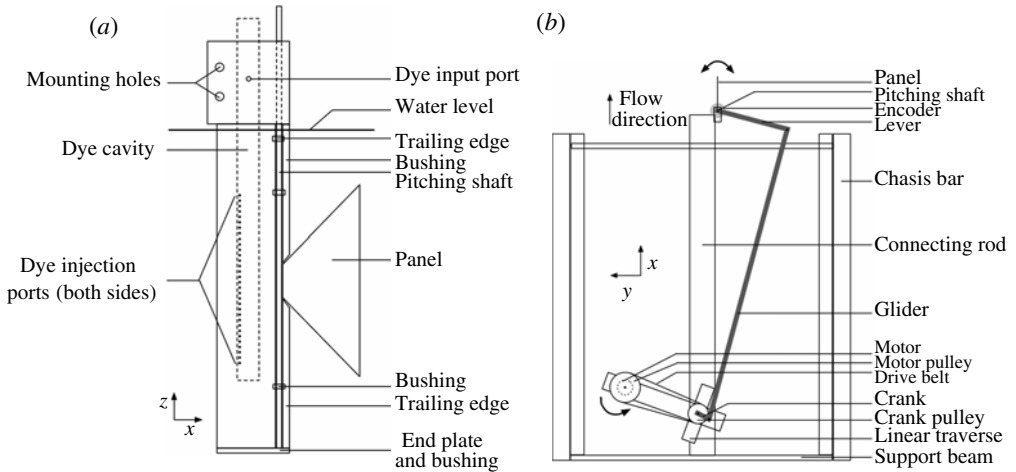FIGURE 1. Trapezoidal panel notation. Flow is from left to right.

FIGURE 2. (*a*) Fairing and panel assembly and (*b*) four-bar linkage mechanism used to actuate the pitching panel. Adapted from Buchholz (2006).

conducted using panels 2 and 3 to further investigate the vortex generation at the diagonal trapezoidal edges of the panels.

3.1. *Digital particle image velocimetry*

Two-dimensional DPIV was acquired in 121 planes uniformly spaced 2 mm apart, oriented normal to the z-direction, as shown in figure 3. The particles used to seed the flow were 13 μm hollow silvered spheres made by Potters Industries Inc. (CONDUCT-O-FIL® SH400S33). The 2 mm thick laser sheet was formed using a Spectra Physics argon-ion laser, a fibre optic cable, collimator and a Powell lens.

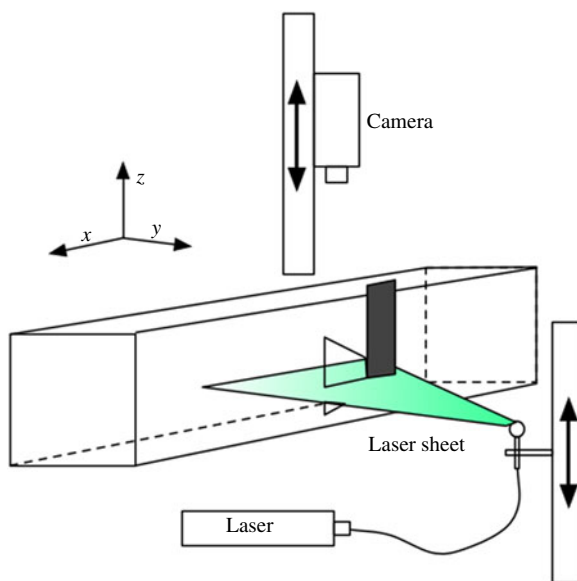|	Panel used	St	Re	A (mm)
3D DPIV	1	0.17, 0.28	4200, 7000	10
2D midspan DPIV	1	0.17–0.56	4200–14 000	20
Flow visualization	2, 3	0.24–0.67	1800–5040	20

TABLE 2. Summary of experimental conditions.

FIGURE 3. (Colour online available at journals.cambridge.org/flm) DPIV acquisition setup.

The Redlake HG-LE camera that was used to acquire the images was mounted vertically above the water channel, as shown in figure 3. To scan the entire measurement volume, the camera and Powell lens were mounted on Velmex X-Slide traverses, controlled by a Velmex VXM stepper motor controller. LabVIEW was used to control the relative positioning of the laser sheet and camera, and the image acquisition at each plane.

Each two-dimensional velocity field was obtained at 25 discrete phases in the pitching cycle. The Redlake camera was externally triggered by a Stanford research systems four-channel digital delay/pulse generator (Model DG535). At each phase, 20 image pairs (Δt between each image: 0.02 s) were acquired, and due to a camera problem that corrupted the first image of each set, 19 of the resulting velocity fields at each phase were phase averaged. This yielded 25 phase-averaged velocity data sets per pitching cycle with a time resolution of 0.04 s.

The extent of each DPIV data set spans 0.24 m ($1.4S$) in spanwise depth, 0.10 m ($1.4c$) in the streamwise direction and 0.15 m ($15A$) in the transverse direction. Full data sets were taken at three overlapping streamwise locations for a total streamwise data length of 0.28 m ($4.1c$). All 121 planes at one streamwise location are shown in figure 4(a), and the resulting overlapping grids from both the upstream and downstream locations are shown in figure 4(b). The streamwise distance is measured

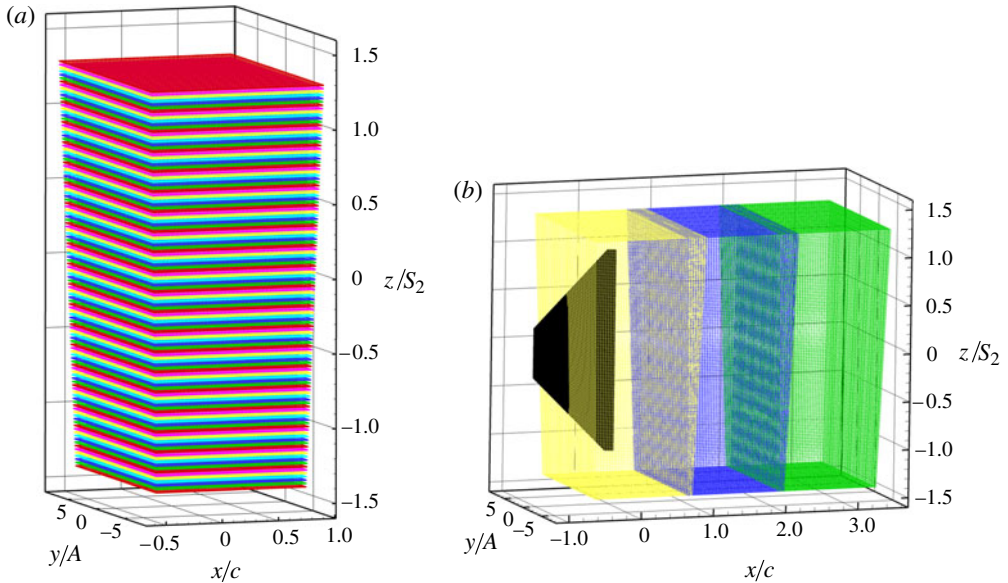FIGURE 4. (Colour online) Two-dimensional DPIV planes and resulting three-dimensional grids.

from the trailing edge and scaled by the panel chord c, so that the upstream edge of the data is located at $x = -0.67c$. The transverse distance is measured from the location of the leading edge and scaled by the pitching amplitude A. The spanwise distance is measured from the midspan and scaled by the trailing edge half-span S_2. These non-dimensionalizations help to clarify the scaling.

The camera was operated at its full resolution of 1128×752 pixels. With the camera and laser sheet aligned to image the deepest spanwise plane, the image resolution was 0.136 mm pixel^{-1}. However, due to the change in refractive index as light travels from water to air, this calibration changed with depth. This effect was handled during post-processing using Snell's law to set the correct image resolution calibration at each plane.

The DPIV analysis in each plane was performed using software developed by Jiménez (2002). A multi-pass cross-correlation algorithm was used, with first 64×64 and subsequently 32×32 pixel window sizes with 50 % overlap. In each of these windows, a two-dimensional Gaussian function was fitted to the correlation peak using five points in the x- and y-directions, providing sub-pixel accuracy in the calculation of pixel displacement.

In general, mean-bias and root-mean-square (r.m.s.) errors from cross-correlation DPIV analyses were of the order of 0.1 pixels (Huang, Dabiri & Gharib 1997). Mean-bias error can occur when the number of particles that remain in the interrogation window is small, which can be caused by insufficient particle seeding or a large ratio of particle displacement to pixel window size. Sources of r.m.s. error can include improper particle seeding, strong velocity gradients and three-dimensional flow causing particles to leave the image plane. Other important factors include non-uniformity in the laser sheet or particle light reflection and electronic noise in the camera or cables. In the current work, the three-dimensional flow, particularly the out-of-plane velocities near the edges of the panel, are assumed to be the largest source of error in the

DPIV experiments. If the out-of-plane velocity (spanwise direction) is assumed to be of the order of the transverse velocity, it will have a maximum value of approximately 50 mm s^{-1}. A particle with this spanwise velocity will travel 1 mm in 0.02 s, the time between each image. Since the laser plane is approximately 2 mm thick, this means that in the regions of the flow where three-dimensional effects are greatest, half the particles in the laser sheet will leave the plane between the first and second images of a pair. The effect on the in-plane velocity calculations will be a decreased magnitude of the correlation peak which increases the r.m.s. error. However, phase averaging the resulting velocity fields mitigates this effect.

Each velocity data set consisted of $132 \times 67 \times 121 = 1\,070\,124$ points, with 8844 points in each spanwise plane. The velocity data grid spacing was 2.2 mm in the (x–y) planes, and, as stated previously, 2 mm in the spanwise (z) direction.

3.2. *Dye flow visualization*

Two forms of dye flow visualization were also used to investigate the large-scale structures of the flow around the rigid trapezoidal panels. White light visualization was used to fully observe the three-dimensional structures, while planar laser-induced fluorescence (PLIF) was used to investigate the structures as they moved through two-dimensional planes. The geometries of panels 2 and 3 were chosen to vary sweep angle but to keep surface area constant. For flow visualization experiments, the trailing edge pitching amplitude (A) was 20 mm, and the Strouhal number was varied by changing the free stream velocity. The dye was injected into the flow through small holes in the aerofoil fairing, visible in figure 2(a). These dye injection ports spanned a 130 mm section of the fairing and, therefore, the width of the dye sheet was 61 % of the trailing edge span of panel 2 and 77 % of the trailing edge span of panel 3. For this reason, interactions of the flow close to the spanwise tips of the trailing edge were not captured with the flow visualization.

For the white light visualization, fluorescein (Sigma-Aldrich 166308) and sulforhodamine B (Sigma-Aldrich 230162) dyes were injected into the hollow cavities of the aerofoil fairing. The fluorescein (green) was injected from the cavity on the right of the fairing ($y > 0$) and the sulforhodamine B (pink) was injected into the left-half cavity ($y < 0$). Images were acquired using a commercial digital camcorder at flow speeds ranging from 0.015 m s^{-1} to 0.042 m s^{-1} with the panel pitching at 0.5 Hz and $A = 20$ mm. This represented Strouhal and Reynolds number ranges of $(0.24 < St < 0.667)$ and $(1800 < Re_c < 5040)$. Dye flow visualization films of these panels were taken from above.

To obtain a more detailed image of the dye flow, PLIF images were taken in a plane normal to both the streamwise flow and the panel surface at four locations along the panel chord: $0.25c$, $0.5c$, $0.75c$ and just downstream of the trailing edge. For these experiments, only the fluorescein dye was injected into one half ($y > 0$) of the aerofoil fairing. The dye was illuminated using the same laser and optics as was used in the DPIV experiments.

In order to image the plane normal to the streamwise direction, a mirror was inserted downstream of the test section at a 45° angle to the free stream flow. Rigid, closed-cell foam was formed into a trailing edge for the angled mirror in order to streamline the shape and reduce flow disturbances. The camera was then positioned at the sidewall of the water channel, as shown in figure 5. White light flow visualization was recorded both before and after the insertion of the mirror, and no appreciable difference in the structure of wake was observed.
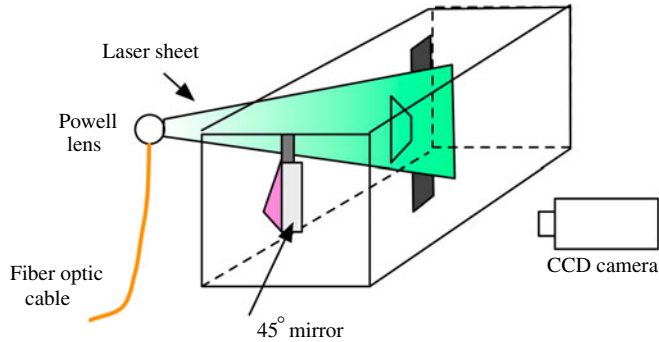
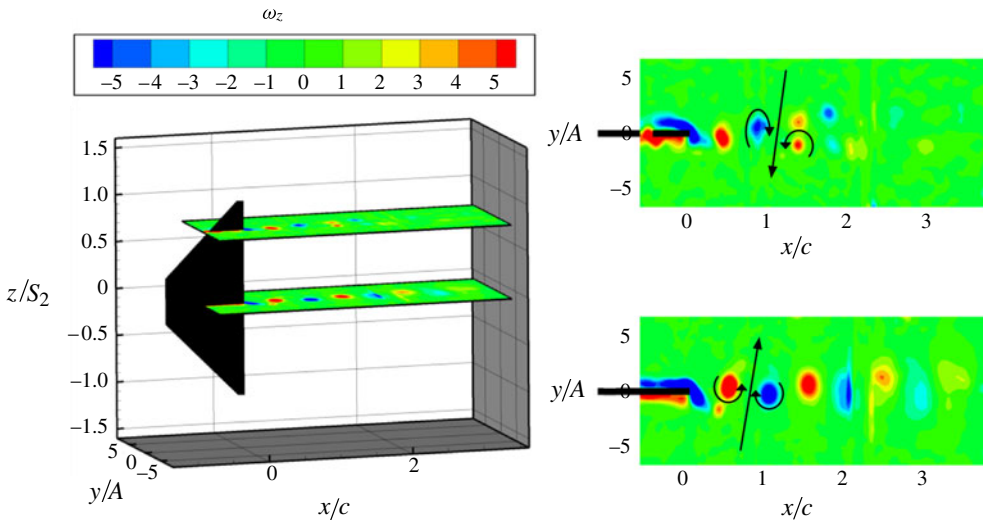FIGURE 5. Schematic of PLIF orientation and setup.

FIGURE 6. Two-dimensional planes of spanwise vorticity in two planes along the span of the trailing edge for $St = 0.17$. Top right: $z = 0.73S_2$; and bottom right: midspan. In all three plots, $\phi = 0°$ with the panel moving either into the page or up. Black arrows indicate direction of vorticity and induced velocity.

4. Results

4.1. *Eulerian wake analysis*

At each point in the volume, velocities in the streamwise (u) and transverse (v) directions were acquired from the DPIV. A second-order accurate central differencing scheme was used to calculate the spatial derivatives of these quantities, and these were in turn used to calculate spanwise vorticity. Figure 6 shows the distribution of the spanwise vorticity ω_z in two planes along the span of the trapezoidal pitching panel at $St = 0.17$. Near the midspan (figure 6, bottom right), the vortices are arranged in a clear 2S, thrust-producing pattern for a distance up to two chord lengths downstream of the trailing edge. The structures are slightly staggered along the transverse centreline and the induced flow between each consecutive vortex pair is directed slightly downstream, adding a small amount of streamwise momentum. While the arrangement of the vortices further downstream still indicates thrust production,
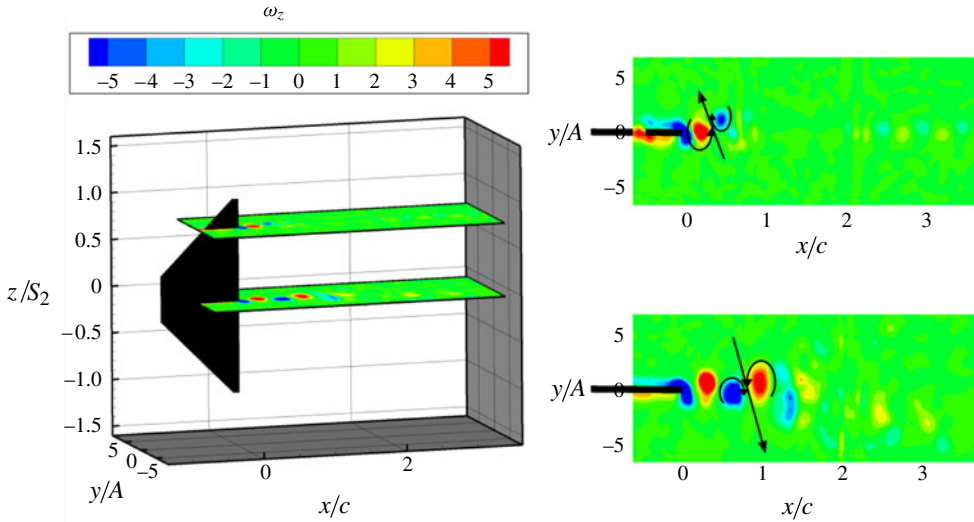
FIGURE 7. Two-dimensional planes of spanwise vorticity in two planes along the span of the trailing edge for $St = 0.28$. Top right: $z = 0.73S_2$; and bottom right: midspan. In all three plots, $\phi = 0°$ with the panel moving either into the page or up. Black arrows indicate direction of vorticity and induced velocity.

the magnitudes of the vorticity peaks lessen and the regions of vorticity concentration become more diffuse.

Away from the midspan near the trailing edge tip (figure 6, top right), the alignment of the vortices shifts and the induced jet between pairs of vortices is directed upstream, indicating a reduction in the streamwise momentum. An appreciable decrease in spanwise vorticity magnitude is also apparent, and more than one chord length downstream the clear 2S pattern that can be seen at the midspan has almost disappeared.

Similar results for $St = 0.28$ are shown in figure 7. At the midspan, the vortices are again aligned to induce velocity downstream, but near the tip they realign so that the streamwise component is in the upstream direction. Some possible reasons for these complicated vortex dynamics away from the midspan are caused by the trapezoidal geometry, and are explored in § 4.3. At the midspan, the 2S vortex configuration is observed to break down approximately one chord length downstream of the trailing edge for this Strouhal number.

For a clearer illustration of the organization of the spanwise vorticity at these two Strouhal numbers, three-dimensional isosurfaces of ω_z are displayed in figures 8 and 9. The results are shown at two phases of motion. At $\phi = 0°$, the panel is crossing the centreline moving into the page, and at $\phi = 180°$, the panel is crossing the centreline moving out of the page.

At $St = 0.17$ (figure 8), the spanwise extent of the wake is contained within the span of the trailing edge, and its extent decreases as the structures move downstream. At $x = 2c$, it is clear that the previously noted loss of vorticity magnitude resembles the vortex breakdown observed further upstream in the higher Strouhal number case. At $St = 0.28$ (figure 9), the spanwise compression of the wake is more exaggerated, and there is also a marked decrease in vorticity magnitude and coherence downstream of $x = c$. It is interesting to note that at the location of the 2S breakdown (for $St = 0.17$,
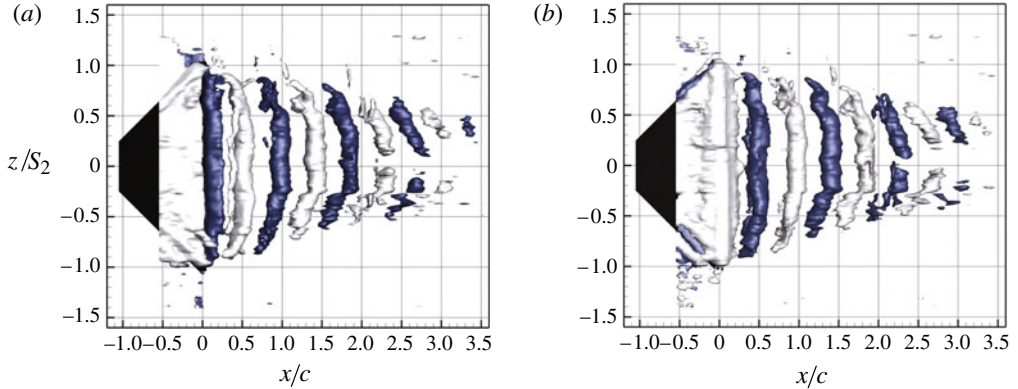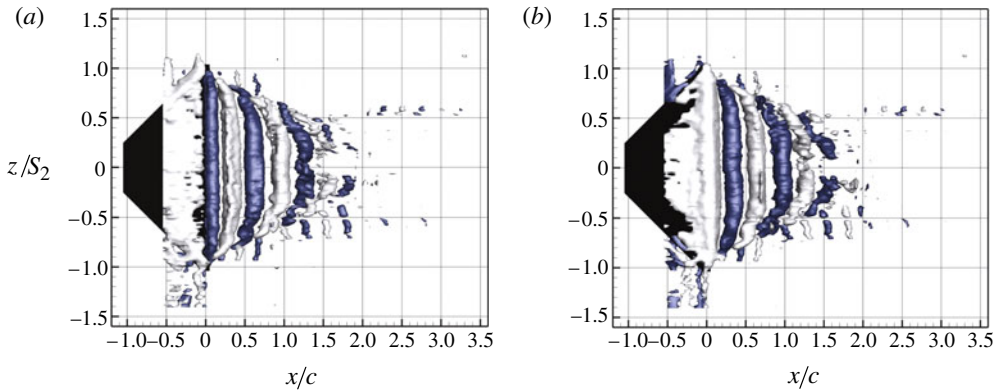
FIGURE 8. (Colour online) Spanwise vorticity for the panel pitching at $St = 0.17$. Light grey and blue (or dark grey in print) surfaces are 14 % of the maximum and minimum ω_z, respectively. (a) $\phi = 0°$ (into the page) and (b) $\phi = 180°$ (out of the page).

FIGURE 9. (Colour online) Spanwise vorticity for the panel pitching at $St = 0.28$. Light grey and blue (or dark grey in print) surfaces are 14 % maximum and minimum ω_z, respectively. (a) $\phi = 0°$ (into the page) and (b) $\phi = 180°$ out of the page.

at $x = 2c$; for $St = 0.28$, at $x = 1.25c$), the spanwise extent of the structures at both Strouhal numbers is approximately the same, extending from $z = -0.5S_2$ to $z = 0.5S_2$. Note that the small spanwise vortices at the edges of the wake that can be seen in the plots of $St = 0.28$, notably in the region ($x > c$, $-0.75S_2 < z < -0.5S_2$), are caused by the shedding from the pitching apparatus as described in § 3.

The evolution of a single vortex as it is shed from the trailing edge and evolves downstream of the trailing edge is shown in figures 10 and 11 for the same two Strouhal numbers. In these plots, the structure is visualized using an isosurface of positive spanwise vorticity. As expected, the individual vortices appear to undergo similar qualitative changes at both Strouhal numbers, only at different distances downstream of the trailing edge. After half a pitching period, the vortex has convected downstream and remains straight for most of its length with the edges curving towards the negative y-direction (figures 10b and 11b). Approximately one period later, the structure is curved along its entire length and there is a pronounced midspan widening of the structure at the higher Strouhal number (figures 10c and 11c). The structure is
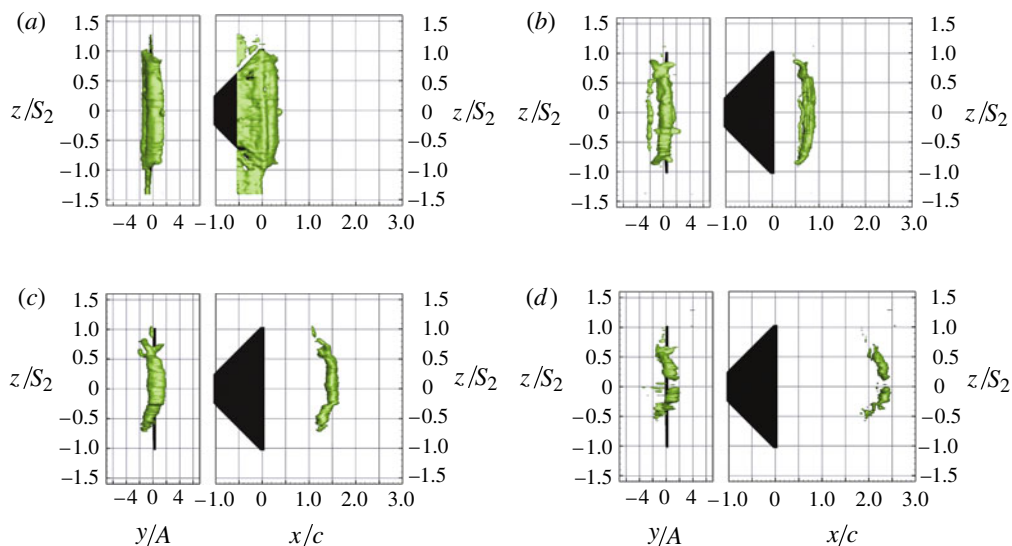
FIGURE 10. (Colour online) Following one vortex as it is shed and evolves downstream (positive spanwise vorticity only, contour level at 13 % of the maximum value); $St = 0.17$. In each subfigure, the left-hand plot shows the view looking upstream, and the right-hand plot is the view looking normal to the direction of pitching. (a) $\phi = 230°$, (b) $\phi = 461°$, (c) $\phi = 749°$ and (d) $\phi = 1095°$.

also curved in the x–z plane as the midspan of the vortex travels downstream faster than the tip. This is consistent with our previous observations from figures 6 and 7, in that the momentum addition occurs at the midspan, not near the spanwise edges.

At the lower Strouhal number, the spanwise vortex is distorted near the spanwise edges, which is can be seen in the upstream view given in figure 10(b). Near $z/S_2 = 0.6$, $-2 < y/A < 2$, it appears that the spanwise structure has split into two symmetric segments. This formation persists to $\phi = 749°$, but is not seen at the higher Strouhal number.

After approximately two and a half pitching periods (figures 10d and 11d), the structure shrinks further and disappears from the figure. There are indications from the results at $St = 0.28$ that the vortex is not actually disappearing at the midspan, but spreading and splitting. Since Eulerian isosurfaces have difficulties tracking the magnitude changes observed here, we employ LCS at the midspan in order to further investigate these three-dimensional effects and the mechanisms of wake breakdown.

4.2. *LCS wake analysis*

The LCS analysis was conducted using the two-dimensional velocity fields obtained in the DPIV experiments. LCS results reveal the outer vortex boundaries, and therefore the full three-dimensional LCS results resemble a shell that obscures the inner details of these structures. The spanwise velocity at the midspan, w, was assumed to be zero, which is expected to be a reasonable assumption for the region of the wake around the midspan where the large-scale structures are expected to be associated primarily with the spanwise vorticity. PLIF images on the panel surfaces and directly behind the panel trailing edge confirm no large-scale asymmetric spanwise fluid motion around the midspan.
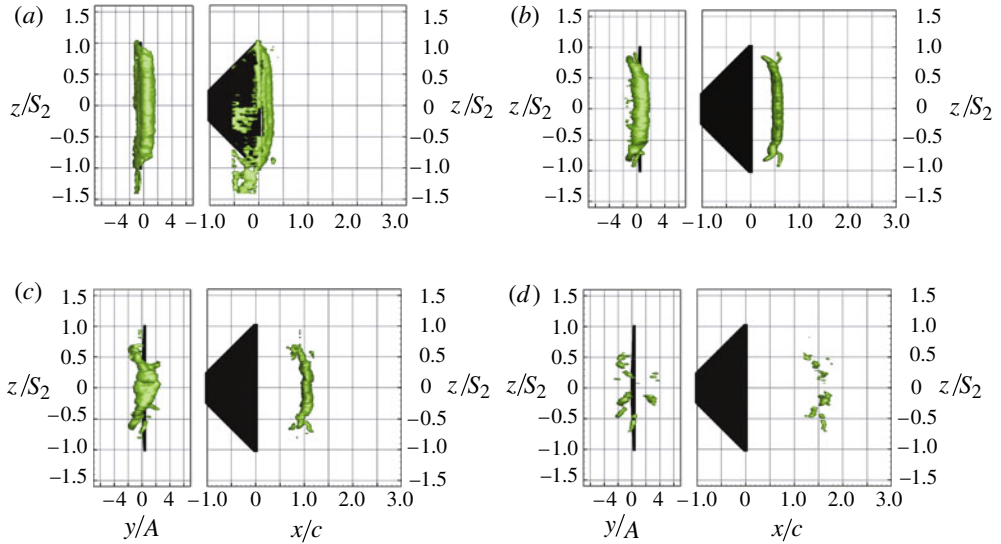
FIGURE 11. (Colour online) Following one vortex as it is shed and evolves downstream (positive spanwise vorticity only, contour level at 13 % of the maximum value). $St = 0.28$. In each subfigure, the left-hand plot shows the view looking upstream, and the right-hand plot is the view looking normal to the direction of pitching. (a) $\phi = 230°$, (b) $\phi = 461°$, (c) $\phi = 749°$ and (d) $\phi = 1095°$.

During the FTLE calculations, particles that left the domain were assumed to travel in the streamwise direction with the free stream velocity. For those trajectories that were advected upstream of the data domain during negative-time calculations, a uniform free stream assumption was reasonable, as this was the boundary condition upstream of the pitching apparatus. Downstream of the data window, however, the loss of information inherent in this assumption causes a lack of sharp ridges in the positive-time FTLE field. This effect is often apparent in the downstream third of the data domain.

Faster computation of the FTLE fields was achieved by exploiting the time-periodic velocity fields and using a 'stitching' process, similar to that described by Brunton & Rowley (2010). Twenty-five short ($T/25$) advection maps which spanned the pitching period were first computed, and then longer advection maps (for the results presented here, $2T$ and $4T$) were acquired by composing the shorter maps.

First we consider the case at $St = 0.17$. The positive- and negative-time FTLE fields in the midspan plane of the wake, calculated using a $2T$ integration time, are shown in figure 12. As expected due to the lack of information downstream, the pFTLE field loses coherence at $x = 2c$, whereas the nFTLE field resembles a two-dimensional wake throughout the field of view. Because the ridges of the FTLE field have negligible mass flux across them, they move with the local velocity field, and continue to roll up in the direction of the local vorticity. The pFTLE, on the other hand, are originally coiled up in the opposite direction from the local vorticity, and unroll as they move with the local velocity field.

The hyperbolicity criteria were applied to the pLCS and nLCS and the resulting structures are shown in figure 13. The LCSs are plotted as regions of the FTLE fields with magnitude greater than 35 % of the maximum. As shown by Green, Rowley & Smits (2010), the boundaries of spanwise vortices consist of time-dependent saddle
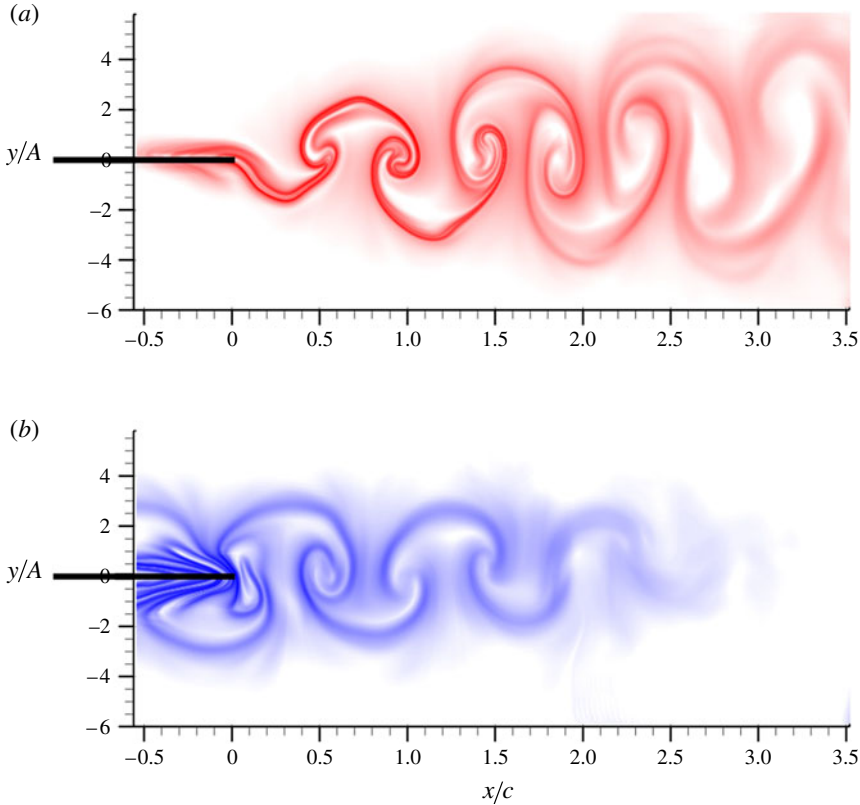
FIGURE 12. nFTLE (top) and pFTLE (bottom) at the midspan of the panel pitching at $St = 0.17$. In both plots, $\phi = 0°$ and the panel is moving up.
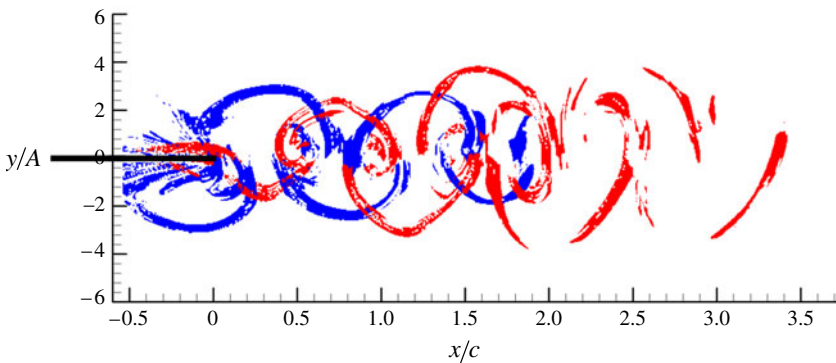

FIGURE 13. Hyperbolic pLCS (blue) and nLCS (red) at the midspan of the panel pitching at $St = 0.17$, $\phi = 0°$ and the panel is moving up. Hyperbolic LCSs are represented by FTLE fields that are blank for values less than 35 % of the maximum of the field, and if the applicable strain criterion is not satisfied.

points at each transverse end of each structure (intersections of the hyperbolic pLCS and nLCS) and an alternating pattern of pLCS and nLCS around the vortex cores.
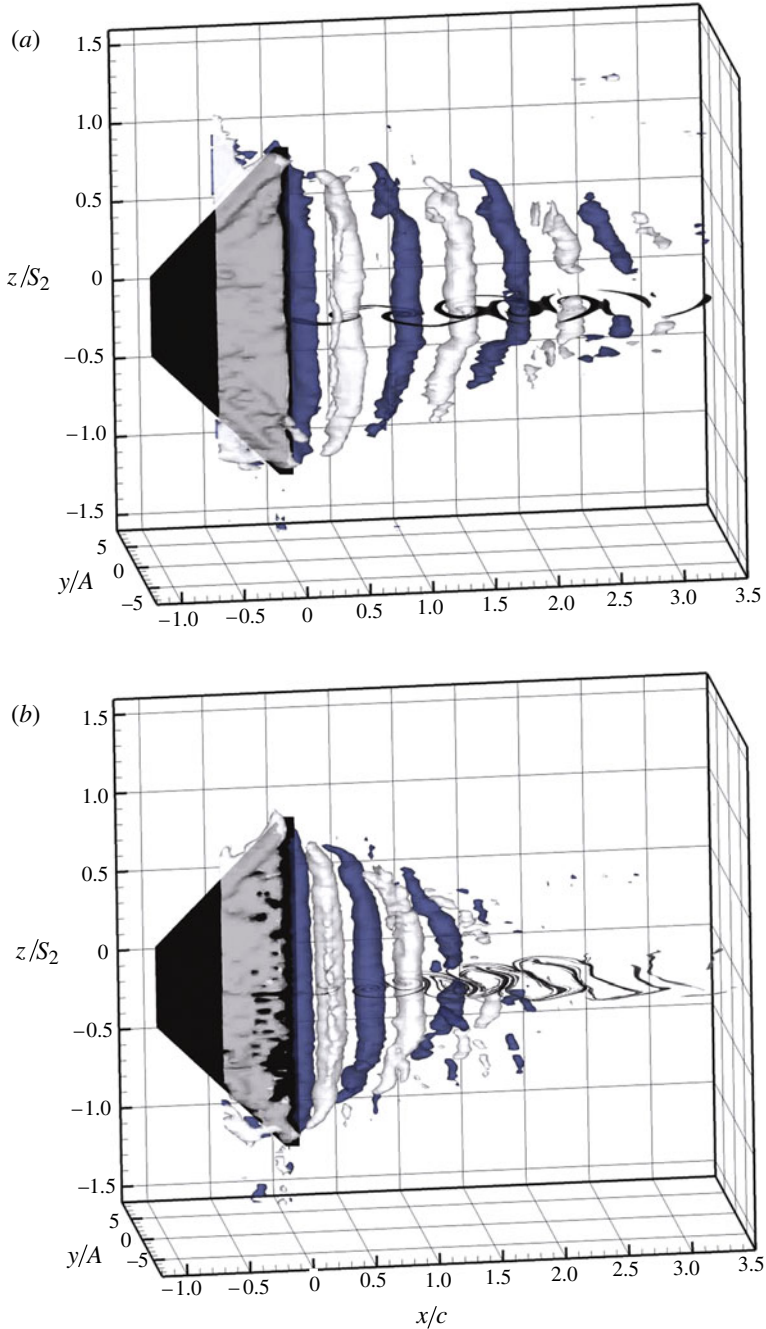
FIGURE 14. (Colour online) Isosurfaces of spanwise vorticity and two-dimensional slices of nFTLE around the panel pitching at (a) $St = 0.17$ and (b) $St = 0.28$. In both figures, $\phi = 0°$ and the panel is pitching into the page. Light grey and blue (or dark grey in print) surfaces are 18 % of the maximum and minimum ω_z, respectively. LCSs are represented by regions where nFTLE > 35 % maximum value at $St = 0.17$ and >46 % at $St = 0.28$.

The spanwise vorticity isosurfaces are plotted simultaneously with the nFTLE ridges in figure 14. It is clear that both the Eulerian and Lagrangian techniques are revealing
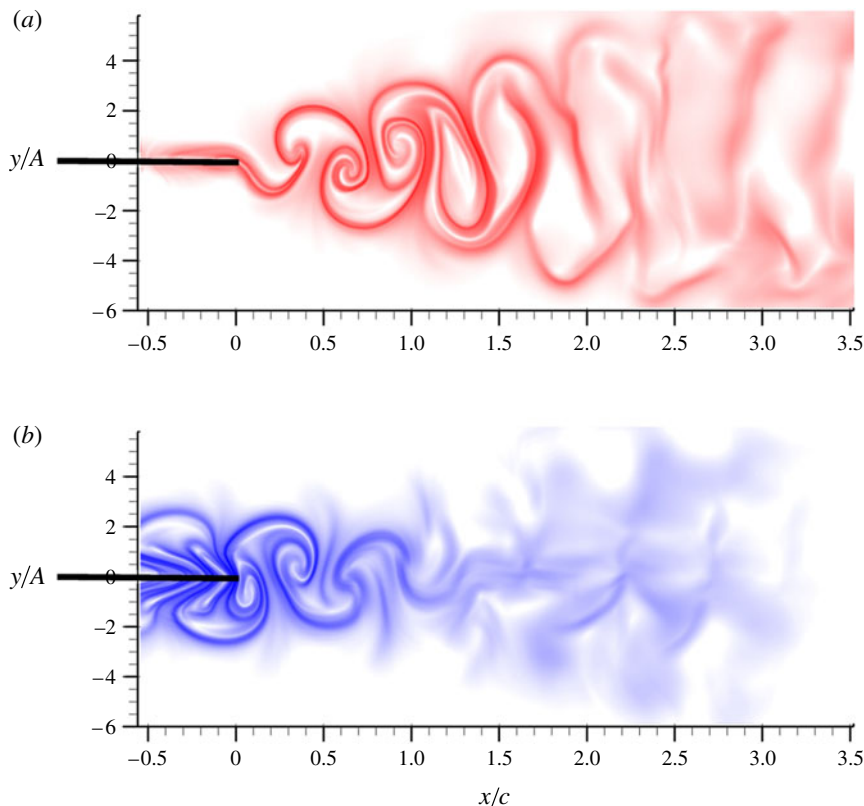
FIGURE 15. (Colour online) nFTLE (top) and pFTLE (bottom) at the midspan of the panel pitching at $St = 0.28$. In both plots, $\phi = 0°$, and the panel is moving up.

the same large-scale structures in the wake. Even near the tip of the panel where the velocity field is expected to be strongly three dimensional, the LCS, calculated by advecting particles constrained to a spanwise-constant plane, nicely captures the local structures marked by the spanwise vorticity component.

Next, we consider the case for $St = 0.28$. The FTLE fields are shown in figure 15. For this Strouhal number, an integration time of $4T$ was used and the pFTLE fields lose coherence downstream of approximately $x = 1.5c$. For $x/c < 1$, the structure of this wake is qualitatively similar to that at the lower Strouhal number, but as the vortices move downstream the pattern becomes increasingly complex.

For a closer look at this transition, the evolution of the hyperbolic pLCS and nLCS at the higher Strouhal number are shown in figure 16. In the near wake, the characteristic pattern of vortex cores bounded by two time-dependent saddles and an alternating pLCS/nLCS boundary is apparent, coinciding with the region where the 2S pattern was clearly observed in the vorticity isosurface plots. However, a qualitative change in the structure of the LCS is seen as the structures evolve. Black circles follow two time-dependent saddle points that bound two distinct vortex cores as they convect downstream. The distance between them decreases until they merge after one pitching cycle. This merger appears to take place just upstream of $1.5c$, which coincides with the breakdown observed in the behaviour of the vorticity isosurfaces.
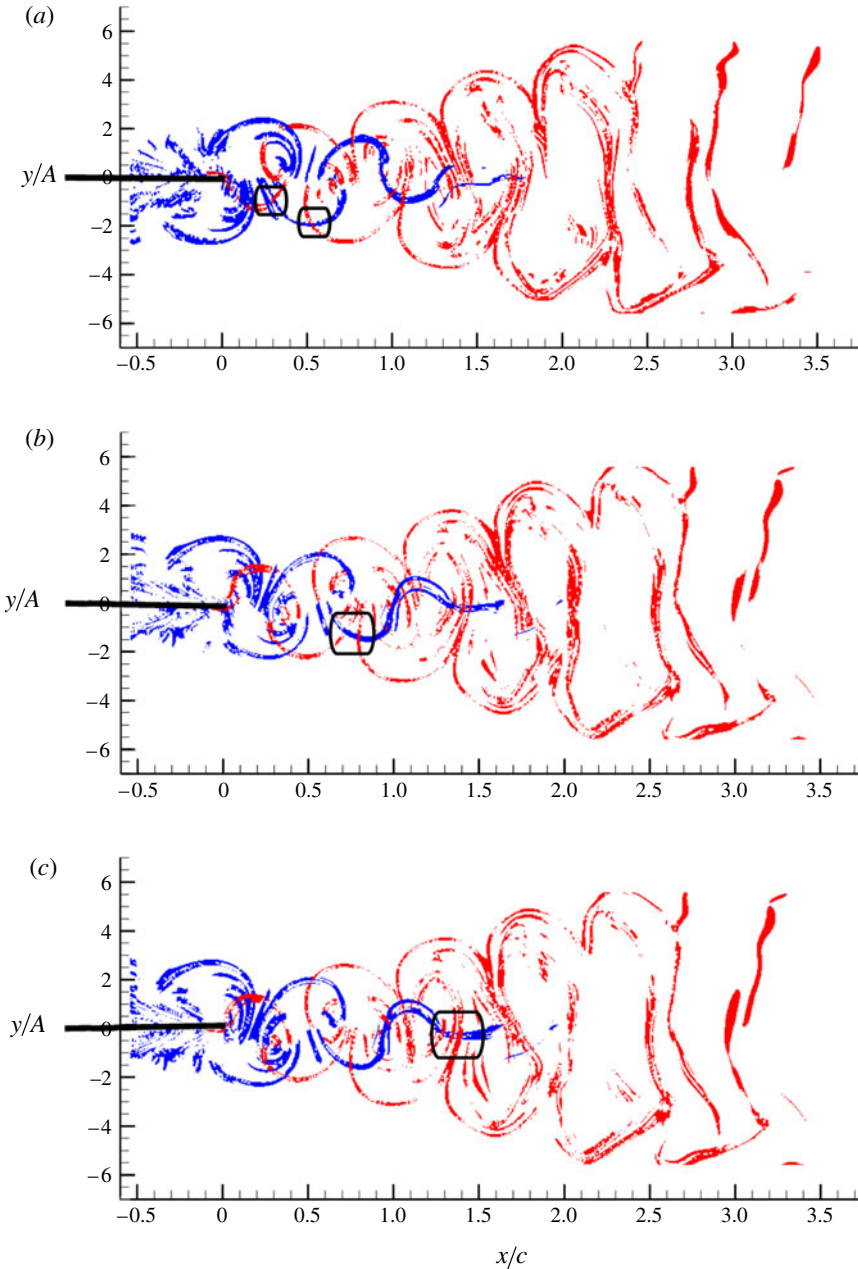
FIGURE 16. Hyperbolic pLCS (blue) and nLCS (red) at the midspan of the panel pitching at $St = 0.28$. Hyperbolic LCSs are represented by FTLE fields that are blank for values less than 46 % of the maximum of the field, and if the applicable strain criterion is not satisfied. (a) $\phi = 0°$ (pitching up), (b) $\phi = 202°$ (pitching down), and (c) $\phi = 533°$ (pitching down).

In figure 17 we investigate the vortex breakdown by simultaneously visualizing the positive vorticity isosurfaces and the midspan LCS at three phases of the panel motion. In each inset on the right-hand side there is an enlarged view of the spanwise structures near the midspan. The isosurfaces are partially transparent to allow the vortex core LCS pattern to be viewed. Because this flow is periodic and only one
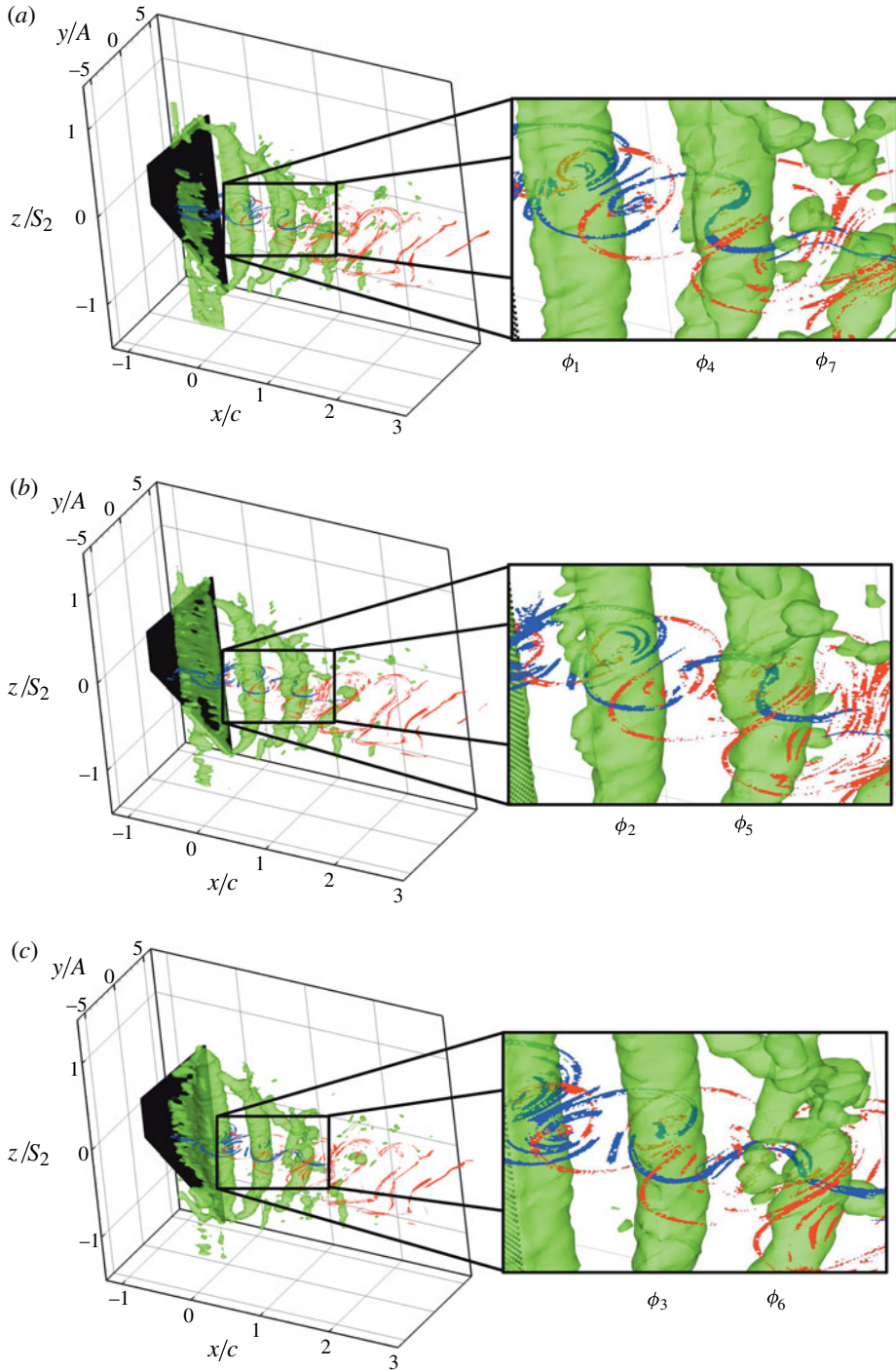
FIGURE 17. Positive vorticity isosurfaces ($14\%\ \omega_{z,max}$) and the midspan hyperbolic LCS (greater than 46% $FTLE_{max}$) at three phases of the panel motion at $St = 0.28$. In each inset on the right-hand side there is an enlarged view of the spanwise structures near the midspan. Seven phases in the evolution of a single vortex are shown, labelled ϕ_1–ϕ_7.

positive vortex is shed during each flapping cycle, the structures labelled (ϕ_1–ϕ_7) represent the same structure at seven phases of the panel motion.

Early in the sequence (ϕ_1–ϕ_3), both the pLCS (blue) and nLCS (red) are rolled up in a scroll pattern in the vortex core. In the enlarged view, it is clear that the pLCS scroll is arranged in a counter-clockwise (CCW) orientation, and the nLCS is in a clockwise orientation. As indicated earlier, the CCW motion of the positive vortices will further coil the nLCS and uncoil the pLCS. At phase ϕ_4, the pLCS that unrolled within the vortex core is hyperbolic along its length and acts as the repelling line that will divide the fluid in the core after the wake breakdown. Indeed, at ϕ_6, the pLCS is aligning with the streamwise flow and the structure begins to split at the midspan. This indicates that this wake breakdown might be a transition to the 2P vortex street, the split wake pattern seen when two pairs of vortices are apparent for each flapping cycle instead of one.

Two-component velocity fields were also obtained at the midspan of the wake with the panel pitching at a higher trailing edge amplitude of $A = 2$ cm for Strouhal numbers in the range $0.17 < St < 0.56$. The pFTLE and nFTLE fields in this plane are shown in figure 18. To display the ridges of both the positive and negative time fields, they are plotted simultaneously, but only where the FTLE value is greater than 25 % of the maximum.

At all but the lowest Strouhal number, we see the signature saddle merger that corresponds to the wake transition downstream of the trailing edge. At $St = 0.26$ the merging of the saddle points must be inferred from the nFTLE ridges due to the downstream loss in fidelity of pFTLE. It can reasonably be assumed that the saddles merge approximately two chord lengths downstream. This distance decreases with increasing St, and is observed to occur at $1 < x/c < 2$ for $St = 0.34$ and at $0.5 < x/c < 1$ for $St = 0.56$. At the smaller pitching amplitude, the transition was observed in both vorticity and LCS plots to occur at approximately $x/c = 1$ for $St = 0.28$ and $x/c > 2$ for $St = 0.17$. At comparable Strouhal number the downstream distance of the transition apparently decreases for smaller pitching amplitudes.

4.3. *Trapezoidal geometry effects*

As mentioned in § 4.1, the trapezoidal geometry induced additional vortex dynamics along the spanwise, or swept, edges of the panel. Figures 19 and 20 show the vorticity contours at both Strouhal numbers in a two-dimensional plane that intersects the swept edge of panel 1. In the left half of figure 19, the panel is pitching up, and creating negative (blue) vorticity at the trailing edge. Vorticity being generated at the swept edge near $x/c = -0.4$ would have a positive spanwise component, and indeed we see a region of positive vorticity (red) that seems to wrap around the upstream panel edge. The vorticity is created by fluid rolling from the top surface toward the bottom, affecting the shape of the boundary layers on both panel surfaces. A half cycle later as the panel pitches down, positive vorticity is shed from the trailing edge and negative vorticity wraps around the swept edge. This same behaviour also occurs at the lower St, although to a lesser degree, as shown in figure 20.

4.3.1. *White light illumination*

The presence of the boundary layers on both sides of the panel makes the swept edge structure difficult to isolate and observe in vorticity plots, and therefore dye flow visualization was used. For these experiments, panels 2 and 3 were pitched with a trailing edge amplitude of $A = 20$ mm, as described in § 3.
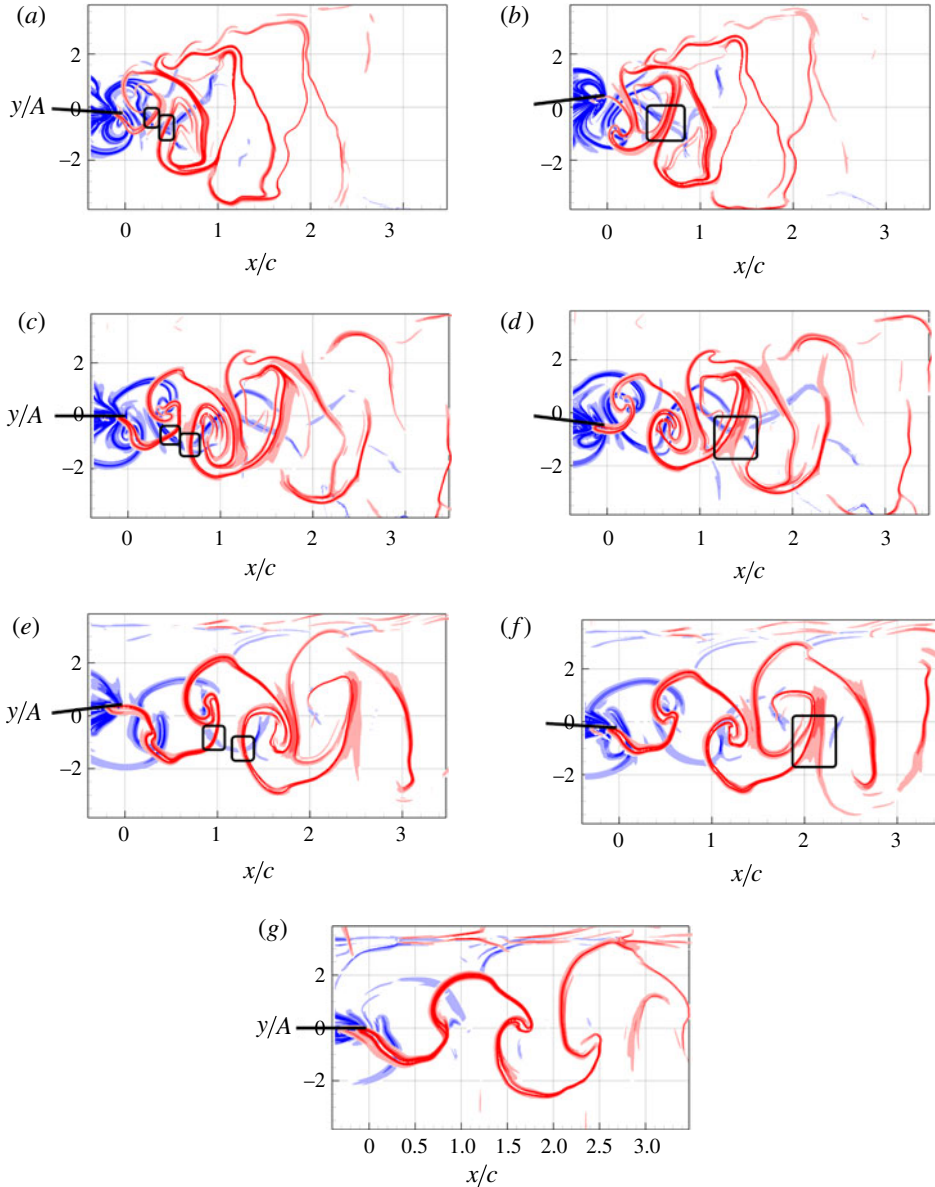
FIGURE 18. nFTLE (red) and pFTLE (blue) ridges at the midspan for a range of St as indicated. FTLE fields are blank for values less than 25 % maximum of the field. (*a*) $St = 0.56, \phi = 331°$; (*b*) $St = 0.56, \phi = 461°$; (*c*) $St = 0.34, \phi = 0°$; (*d*) $St = 0.34, \phi = 274°$; (*e*) $St = 0.26, \phi = 72°$; (*f*) $St = 0.26, \phi = 331°$ and (*g*) $St = 0.17, \phi = 0°$.

Figure 21(*a*) shows a top view of white light illuminated dye in the flow field around panel 2 with $St = 0.33$. There is a clear organization of the dye on the top and bottom surfaces of the panel. In particular, in figure 21(*a*) one organized structure is observed on the bottom surface and two are observed on the top surface. Each structure is marked by both the green fluorescein and pink rhodamine dyes that were
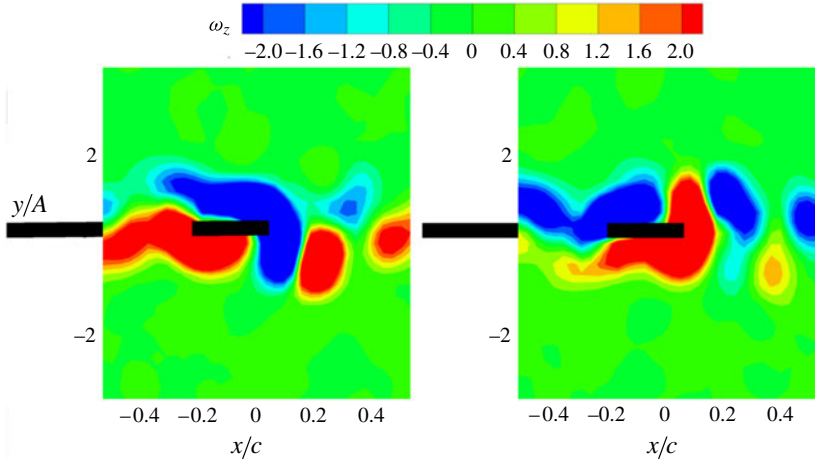
FIGURE 19. Spanwise vorticity in a two-dimensional plane located at $z = 0.84S_2$ for panel 1 pitching at $St = 0.28$. Left: $\phi = 0°$; and right: $\phi = 180°$. The two-dimensional plane location along the panel is similar to that in figure 7.
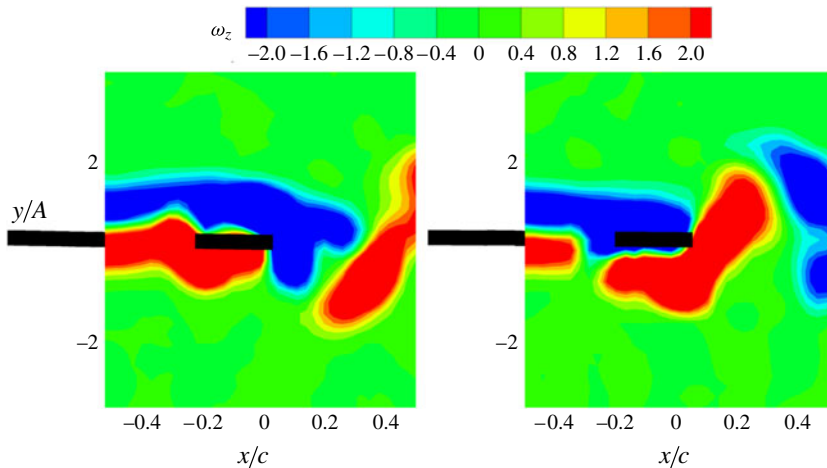

FIGURE 20. Spanwise vorticity in a two-dimensional plane located at $z = 0.84S_2$ for panel 1 pitching at $St = 0.17$. Left: $\phi = 0°$; and right: $\phi = 180°$. The two-dimensional plane location along the panel is similar to that in figure 6.

injected from opposite sides of the fairing. These are the vortices rolling up around the swept edges of the trapezoidal panel, and therefore they entrain dyes from both sides of the swept edge.

As the Strouhal number is increased by decreasing the free stream velocity, this organization of the dye does not persist. In figure 21(*b*), the Strouhal number has been increased to 0.42, and while there is still some coherence in the dye pattern around panel 2, the packets are closer together and boundaries become less clear. When the Strouhal number is increased to 0.55, shown in figure 21(*c*), all coherence is lost.
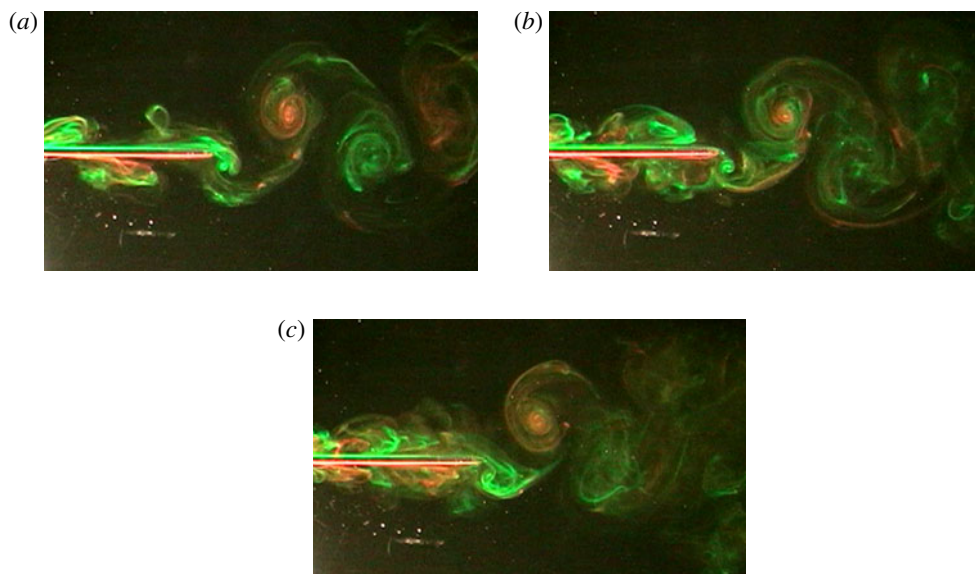
FIGURE 21. White light flow visualization of panel 2 pitching at three Strouhal numbers, viewed from above at $\phi \approx 0°$ (pitching up). (*a*) $St = 0.33$, (*b*) $St = 0.42$ and (*c*) $St = 0.55$.

4.3.2. *Planar laser-induced fluorescence*

The swept edge structure is more clearly seen using PLIF. Figure 22 shows PLIF images acquired at $x = 0.25c$ at four phases of motion of panel 2 with $St = 0.33$. This view is from downstream of the panel looking upstream, and in this view swirling dye flow marks the streamwise component of vorticity. In figure 22(*a*), the panel is at the right-most extremum, and the dye clearly marks the creation of a counter-rotating vortex pair on the left-hand side of the panel surface. This vortex pair has a component in the streamwise direction, but it is also expected to have a component in the spanwise direction, since it is aligned with the swept edge. Green & Smits (2008) measured time-resolved pressures on a similarly actuated rectangular pitching panel, and saw a strong pressure differential between the two sides of the panel exists at the extremes of the panel motion. Here, on the trapezoidal panel, we infer that, half a period earlier, a similar pressure difference drew fluid from what was the advancing surface (right) to the retreating surface (left). The fluid rolls around the swept edge, and the vortex pair is created as it impinges on the panel surface.

Figure 22(*b*) shows that this vortex pair persists as the panel turns and moves through the zero angle of attack moving to the left. By the time it has reached the left-most extremum (figure 22*c*), a similar pair has been created on what will become the advancing surface (right) of the panel. This structure also persists as the panel sweeps to the right (figure 22*d*).

The swept edge structure retains its coherence as it convects along the panel surface. In figure 23, we show PLIF images at four locations along the panel chord, at phases chosen so that the swept edge structure generated at $x \approx 0.25c$ passes through the laser plane. Similar vortex roll-ups at the edge are not observed downstream of $x = 0.25c$ due to the limited spanwise extent of the dye injection. At $x = 0.5c$ (figure 23*b*), the counter-rotating vortices generated upstream are observed one half pitching period later. At this location, they have spread apart in the spanwise direction, but as they
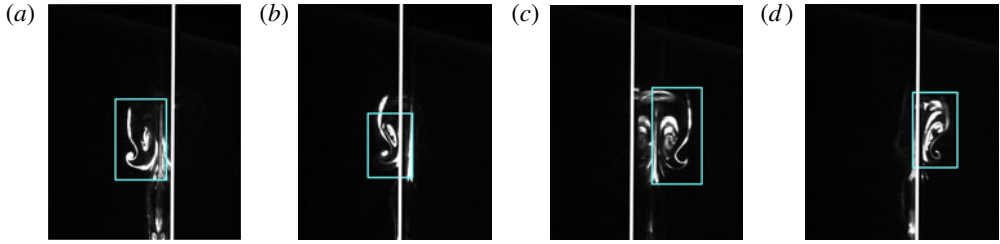
FIGURE 22. (Colour online) PLIF images on panel 2 pitching at $St = 0.33$, acquired at $x = 0.25c$. Boxes highlight counter-rotating vortex pairs rolling up at the swept edge, and a vertical white line indicates the position of the trailing edge. (*a*) $\phi \approx 90°$, (*b*) $\phi \approx 180°$, (*c*) $\phi \approx 270°$ and (*d*) $\phi \approx 360°$.
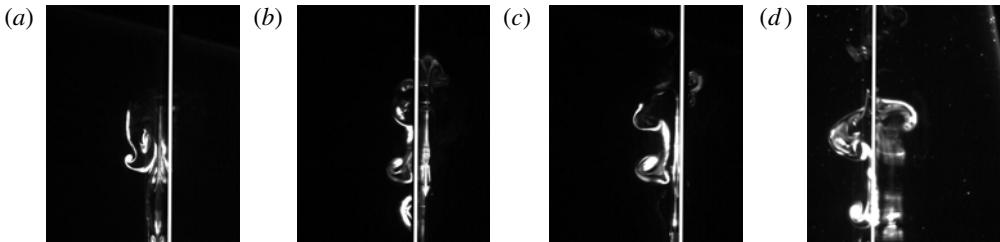

FIGURE 23. PLIF images on panel 2 pitching at $St = 0.33$, acquired at different streamwise locations along the chord. Phases are chosen to correspond to the crossing of the swept edge structure through the laser plane. A vertical white line indicates the position of the trailing edge. (*a*) $x = 0.25c$, $\phi \approx 135°$, (*b*) $x = 0.5c$, $\phi \approx 310°$, (*c*) $x = 0.75c$, $\phi \approx 450°$ and (*d*) $x \approx c$, $\phi \approx 480°$.
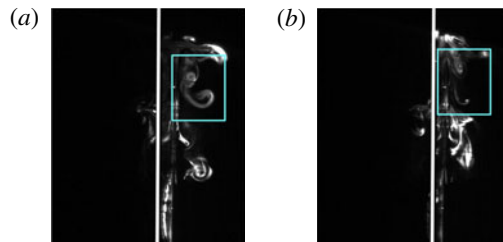

FIGURE 24. (Colour online) PLIF images on panel 2 pitching at $St = 0.55$, acquired at $x = 0.5c$. Boxes highlight the quasi-streamwise structure as it is created and then pulled over the swept edge, and a vertical white line indicates the position of the trailing edge. (*a*) $\phi \approx 270°$ and (*b*) $\phi \approx 315°$.

move downstream (figure 23*c*) their relative distance does not continue to increase. Just downstream of the trailing edge, the structure generated at the swept edge at $0.25c$ retains its shape, and is being shed into the wake (figure 23*d*) approximately one pitching period later. The column of dye seen to the right of the panel trailing edge marker is the cross-section of the spanwise vortex simultaneously being shed from the trailing edge.
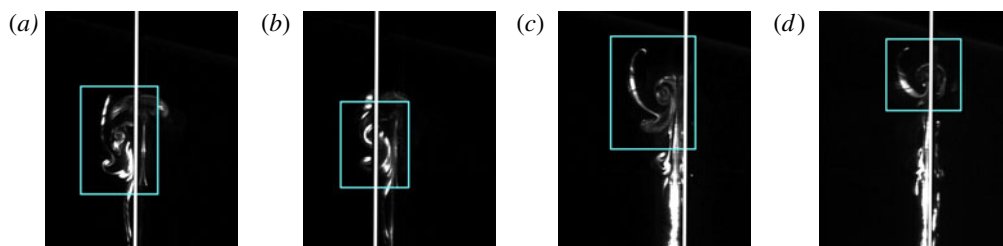
FIGURE 25. (Colour online) PLIF images of swept edge structure roll-up on panel 2 (at $x = 0.25c$, $St = 0.42$) and panel 3 (at $x = 0.5c$, $St = 0.42$). The box highlights the structure of interest. (*a*) Panel 2, $\phi \approx 180°$, (*b*) panel 2, $\phi \approx 270°$, (*c*) panel 3, $\phi \approx 90°$ and (*d*) panel 3, $\phi \approx 180°$.

PLIF images were also acquired with the panel pitching at $St = 0.55$, and these are shown in figure 24. It is clear that a vortex pair rolled up along the swept edge as the panel moved from right to left. However, as the panel decelerates, this pair does not continue to develop, and instead interacts with the swept edge. From Green & Smits (2008) we infer that at this point in the phase the pressure on the advancing surface of a rectangular pitching panel is high, with a favourable gradient toward the spanwise edges. This favourable pressure gradient will induce the flow toward the edges, and break up the swept edge structures. In figure 24(*b*), it can be seen that this structure is already being pulled over the swept edge and losing coherence. Downstream of the trailing edge, no coherent streamwise structures were observed.

We refer to the behaviour of the swept edge structure at lower Strouhal numbers, especially with regard to its continued coherence down the panel and in the wake, as 'structure trapping'. This phenomenon was observed to depend not only on the Strouhal number, which was varied by changing the free stream velocity, but on the panel geometry as well. For example, flow visualization was also acquired for a trapezoidal panel with swept edges at a smaller angle to the free stream (panel 3). PLIF images acquired on both panels pitching at $St = 0.42$ are shown in figure 25. The swept edge structure generated at $x = 0.25c$ on panel 2 retains coherence and is 'trapped' on the left surface as the panel sweeps from right to left.

Images at $x = 0.5c$ on panel 3 are shown in figure 25(*c*,*d*). In this case, a similar quasi-streamwise structure is created, but as the panel sweeps from right to left it is pulled over the swept edge, and no trapping occurs. However, trapping was observed to occur on panel 3 for $St < 0.37$. Trapping was observed on panel 2 for $St < 0.47$. The swept edge structure trapping occurred when either the free stream velocity is increased or the swept edge angle is increased.

To explain how these structures are trapped, a schematic of the swept edge structure dynamics is shown in figure 26. The swept edge structures outlined by the ovals were created in the previous half-cycle, as the panel pitched into the page. In the current half-cycle, as the panel pitches out of the page, they have convected downstream along the panel surface. It is expected that structure trapping occurs when the vortex has travelled far enough away from the swept edge such that it does not interact with the edge in the subsequent half-cycle. The 'edge distance' in this half-cycle, indicated by a line in figure 26, can be increased in two ways: by decreasing the Strouhal number or by increasing the sweep angle of the panel edge. Between panels 2 and 3 at the same free stream velocity, swept edge structures will achieve a larger edge distance on
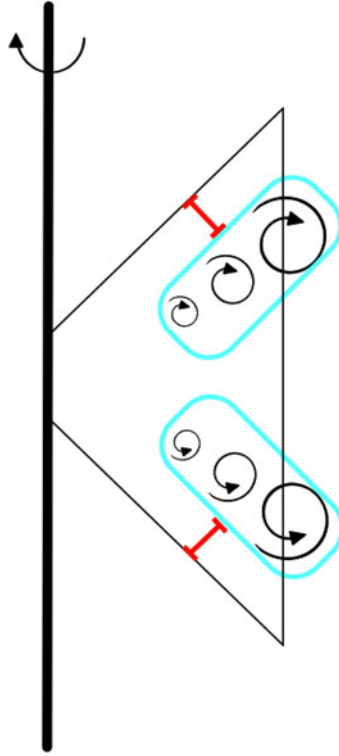
FIGURE 26. (Colour online) Schematic of quasi-streamwise structure dynamics. The structure is outlined in blue (grey in print), distance from the swept edge is indicated with the red (black in print) I bars.

panel 2 due to the larger sweep angle. Therefore, a higher free stream velocity (lower St) was needed for the same phenomenon to occur on panel 3.

5. Discussion

Previous work has shown that low-aspect-ratio pitching propulsors, used to model simple caudal fin swimming, produce a range of wake structures. Specifically, both thrust- and drag-producing 2S vortex streets, where two single vortices are shed from the trailing edge each flapping cycle, and 2P streets, where two pairs are shed each cycle, have been observed with changing Strouhal number. In the current work, two-component DPIV was acquired at two Strouhal numbers throughout the volume of the three-dimensional wake of a low-aspect-ratio trapezoidal panel.

Images of spanwise vorticity revealed a realignment of the vorticity from the midspan to the edges of the wake. At the midspan, vortices were organized in a thrust-producing formation, whereas drag production was apparent closer to the tips of the trapezoidal panel. For these low-aspect-ratio propulsors, the total integrated behaviour of the wake cannot be inferred from analysis performed solely at the midspan. Experimental force measurements or three-component velocity fields would be necessary to determine the quantitative thrust performance of the panels discussed here.

The structure of the wake away from the midspan was difficult to describe fully from the spanwise vorticity information presented here because vorticity in both the streamwise and transverse directions became important. The geometry of the trapezoidal panel complicates matters further. Previous work that studied the wake of a rectangular panel showed that structures created at the spanwise edges are aligned with the free stream direction, and mostly stretch and convect parallel to the edge of the panel. The spanwise edge of the trapezoidal panel, however, cuts across the travel path of those structures which roll up along its length. At the higher *St*, where we have lower free stream velocity, structures created at the swept edge would not convect far from the edge, and continually interact with it.

At higher convective speeds (and therefore lower *St*), however, there was the possibility that structures generated at these swept edges could shed and become 'trapped', retaining some coherence as they travelled along the panel surface toward the trailing edge. Because the trapped vortices were aligned diagonally and had components both parallel and normal to the spanwise trailing edge structures, the interaction would not only distort the structures near the spanwise edges of the wake, but there could be either constructive or destructive interference as well. The fact that this phenomenon occurs at a Strouhal number closer to that at which real fish swim, and that it is not observed on panels of rectangular planform, might indicate an advantage of trapezoidal geometry.

Near the midspan at both Strouhal numbers, a 2S formation was present in the near wake, but farther downstream there was a loss of vorticity magnitude and the wake began to expand in the transverse direction. At $St = 0.28$, these effects were more apparent and occurred further upstream. In addition, three-dimensional plots of spanwise vorticity showed a clear compression of the structures as they travelled downstream. Isolated isosurfaces revealed that each vortex also curves in the transverse direction, consistent with the spanwise realignment observed in the vorticity plots. This indicated that strong interactions at the vortex tips, along with spanwise shortening and structure contortion, corresponded to the observed spreading and disintegration of vorticity.

Lagrangian coherent structures revealed the characteristic pattern of a vortex street around the 2S vortex cores, as discussed previously in Green *et al.* (2010). The boundaries of these vortices, as indicated by the LCS, aligned with the structures observed in the vorticity plots. The LCS curves, however, are largely independent of the threshold value used to plot them. Whereas vortex cores grow and shrink significantly as the vorticity threshold is changed, the boundaries provided by LCSs only thicken or thin slightly.

At the higher Strouhal number, a loss of the characteristic LCS vortex core pattern was observed to coincide with the structure breakdown seen in the vorticity plots. In particular, two saddle points that belonged to the boundaries of two distinct vortices appeared to merge at the location of splitting while the repelling material line (pLCS) unravelled and persisted as a separatrix aligned with the streamwise flow, indicating that downstream of this point the wake split into a quasi-2P street.

This phenomenon was shown to occur at the midspan of wakes for a range of Strouhal numbers and at two trailing edge pitching amplitudes. At constant amplitude, the transition point moved upstream with increasing Strouhal number (decreasing velocity). Interestingly, at comparable Strouhal number, the transition was also observed to occur earlier with smaller amplitude (decreasing velocity), but at constant velocity an increase in amplitude (and, hence, Strouhal number) resulted in an earlier transition. Therefore, increasing the velocity and decreasing the amplitude will

both deter transition, but the non-dimensional parameter that governs this behaviour is more complex than the Strouhal number alone.

With an increasing Strouhal number and constant pitching amplitude, the time scale of the trailing edge vortex shedding decreases relative to the time scale of the convective flow. At higher Strouhal number, the structures were closer to each other in the wake, encouraging interaction and accelerating the transition or splitting of the wake from a 2S to the possible 2P vortex street. While this wake transition was inferred from the vorticity plots, the use of the LCS provided a quantifiable way to identify this transition to the pattern often observed in nature.

REFERENCES

BORAZJANI, I. & SOTIROPOULOS, F. 2008 Numerical investigation of the hydrodynamics of anguilliform swimming in the transitional and inertial flow regimes. *J. Expl Biol.* **212**, 576–592.

BRUNTON, S. L. & ROWLEY, C. W. 2010 Fast computation of finite-time Lyapunov exponent fields for unsteady flows. *Chaos* **20**, 017503.

BUCHHOLZ, J. H. J. 2006 The flowfield and performance of a low aspect ratio unsteady propulsor. PhD the, Princeton University.

BUCHHOLZ, J. H. J., GREEN, M. A. & SMITS, A. J. 2011 Circulation of vortices generated by a pitching panel. *J. Fluid Mech.* (in press).

BUCHHOLZ, J. H. J. & SMITS, A. J. 2008 The wake structure and thrust performance of a rigid low-aspect-ratio pitching panel. *J. Fluid Mech.* **603**, 331–365.

CHONG, M. S., PERRY, A. E. & CANTWELL, B. J. 1990 A general classification of three-dimensional flow fields. *Phys. Fluids* A **2** (5), 765–777.

CLARK, R. P. & SMITS, A. J. 2006 Thrust production and wake structure of a batoid-inspired oscillating fin. *J. Fluid Mech.* **562**, 415–429.

DABIRI, J. O. 2009 Optimal vortex formation as a unifying principle in biological propulsion. *Annu. Rev. Fluid Mech.* **41**, 17–33.

DONG, H., MITTAL, R., BOZHURTTAS, M. & NAJJAR, F. 2005 Wake structure and performance of finite aspect-ratio flapping foils. In *43rd AIAA Aerospace Sciences Meeting and Exhibit*. AIAA.

ELDREDGE, J. D. & CHONG, K. 2010 Fluid transport and coherent structures of translating and flapping wings. *Chaos* **20**, 017509.

VON ELLENRIEDER, K. D., PARKER, K. & SORIA, J. 2003 Flow structures behind a heaving and pitching finite-span wing. *J. Fluid Mech.* **490**, 129–138.

GHOVARDHAN, R. & WILLIAMSON, C. H. K. 2005 Vortex-induced vibrations of a sphere. *J. Fluid Mech.* **531**, 11–47.

GREEN, M. A., ROWLEY, C. W. & HALLER, G. 2007 Detection of Lagrangian coherent structures in three-dimensional turbulence. *J. Fluid Mech.* **572**, 111–120.

GREEN, M. A., ROWLEY, C. W. & SMITS, A. J. 2010 Using hyperbolic Lagrangian coherent structures to investigate vortices in bioinspired fluid flows. *Chaos* **20**, 017510.

GREEN, M. A. & SMITS, A. J. 2008 Effects of three-dimensionality on thrust production by a pitching panel. *J. Fluid Mech.* **615**, 211–220.

GUGLIELMINI, L. 2004 Modeling of thrust generating foils. PhD thesis, University of Genoa.

HALLER, G. 2002 Lagrangian coherent structures from approximate velocity data. *Phys. Fluids* **14** (6), 1851–1861.

HALLER, G. 2005 An objective definition of a vortex. *J. Fluid Mech.* **525**, 1–26.

HALLER, G. 2010 A variational theory of hyperbolic Lagrangian coherent structures. *Physica* D (in press).

HALLER, G. & YUAN, G. 2000 Lagrangian coherent structures and mixing in two dimensional turbulence. *Physica* D **147**, 352–370.

HUANG, H., DABIRI, D. & GHARIB, M. 1997 On errors of digital particle image velocimetry. *Meas. Sci. Technol.* **8**, 1427–1440.

HULTMARK, M., LEFTWICH, M. & SMITS, A. J. 2007 Flowfield measurements in the wake of a robotic lamprey. *Exp. Fluids* **43**, 683–690.

HUNT, J. C. R., WRAY, A. A. & MOIN, P. 1988 Eddies, stream, and convergence zones in turbulent flows. *Center for Turbulence Research Rep.* CTR-S88.

JEONG, J. & HUSSEIN, F. 1995 On the identification of a vortex. *J. Fluid Mech.* **285**, 69–94.

JIMÉNEZ, J. M. 2002 Low reynolds number studies in the wake of a submarine model using particle image velocimetry. Master's thesis, Princeton University.

KOOCHESFAHANI, M. M. 1989 Vortical patterns in the wake of an oscillating airfoil. *AIAA J.* **27** (9), 1200–1205.

LAPEYRE, G. 2002 Characterization of finite-time Lyapunov exponents and vectors in two-dimensional turbulence. *Chaos* **12** (3), 688–698.

LAUDER, G. V. & TYTELL, E. D. 2006 Hydrodynamics of undulatory propulsion. In *Fish Biomechanics* (ed. R. E. Shadwick & G. V. Lauder). *Fish Physiology, vol. 23*. pp. 425–468. Academic.

LEKIEN, F. & LEONARD, N. 2004 Dynamically consistent Lagrangian coherent structures. In *American Inst. of Physics: 8th Experimental Chaos Conference*, CP 742, pp. 132–139.

LIPINSKI, D., CARDWELL, B. & MOHSENI, K. 2008 A Lagrangian analysis of a two-dimensional airfoil with vortex shedding. *J. Phys.* A: Math. Theor. **41**, 1–22.

O'FARRELL, C. & DABIRI, J. O. 2010 A Lagrangian approach to identifying vortex pinch-off. *Chaos* **20**, 017513.

SARKAR, S. & VENKATRAMAN, K. 2006 Numerical simulation of thrust generating flow past a pitching aerofoil. *Comput. Fluids* **35**, 16–42.

SHADDEN, S. C., DABIRI, J. O. & MARSDEN, J. E. 2006 Lagrangian analysis of fluid transport in empirical vortex ring flows. *Phys. Fluids* **18**, 047105–1–047105–11.

SHADDEN, S. C., LEKIEN, F. & MARSDEN, J. E. 2005 Definition and properties of Lagrangian coherent structures from finite-time Lyapunov exponents in two-dimensinal aperiodic flows. *Physica* D **212**, 271–304.

SHADDEN, S. C., ASTORINO, M. & GERBEAU, J.-F. 2010 Computational analysis of an aortic valve jet with Lagrangian coherent structures. *Chaos* **20**, 017512.

SHADDEN, S. C., KATIJA, K., ROSENFELD, M., MARSDEN, J. E. & DABIRI, J. O. 2007 Transport and stirring induced by vortex formation. *J. Fluid Mech.* **593**, 315–331.

SHADDEN, S. C. & TAYLOR, C. A. 2008 Characterization of coherent structures in the cardiovascular system. *Ann. Biomed. Engng* **36** (7), 1152–1162.

TANG, W., CHAN, P. W. & HALLER, G. 2010 Accurate extraction of Lagrangian coherent structures over finite domains with application to flight data analysis over Hong Kong International Airport. *Chaos* **20**, 017502.

TRIANTAFYLLOU, G., TRIANTAFYLLOU, M. & GROSENBAUGH, M. 1993 Optimal thrust development in oscillating foils with application to fish propulsion. *J. Fluids Struct.* **7** (2), 205–224.

TYTELL, E. D., BORAZJANI, I., SOTIROPOULOS, F., BAKER, T. V., ANDERSON, E. J. & LAUDER, G. V. 2010 Disentangling the functional roles of morphology and motion in the swimming of fish. *Integr. Compar. Biol.* **50** (6), 1140–1154.

WILLIAMSON, C. H. K. & ROSHKO, A. 1988 Vortex formation in the wake of an oscillating cylinder. *J. Fluids Struct.* **2**, 355–381.

ZHOU, J., ADRIAN, R. J., BALACHANDAR, S. & KENDALL, T. M. 1999 Mechanisms for generating coherent packets of hairpin vortices in channel flow. *J. Fluid Mech.* **387**, 353–396.

ZHU, Q. & SHOELE, K. 2008 Propulsion performance of a skeleton-strengthened fin. *J. Expl Biol.* **211**, 2087–2100.